Cell Reports
Physical Science

CellPress
OPEN ACCESS

Article

A filterless organic photodetector electrically switchable between visible and infrared detection

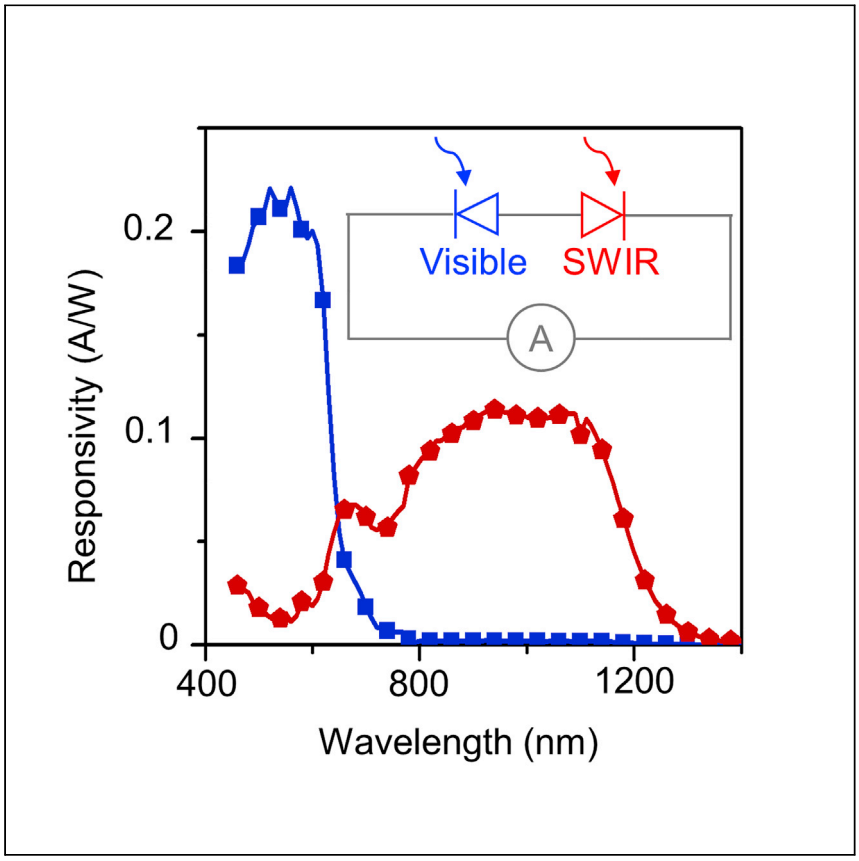

Li et al. report an organic dual-band photodetector with a switchable response to visible and IR spectral regions. The rapid response of tens of kHz is enabled by simple voltage control of <1 V. The device is based on back-to-back diodes, a configuration that may be generalizable to other thin-film optoelectronic materials.

Ning Li, Naresh Eedugurala, Jason D. Azoulay, Tse Nga Ng

tnn046@ucsd.edu

Highlights

Bias-switchable photodetection between visible and infrared sensing

Back-to-back diodes designed for tuning spectral ranges

Response speed of 18 kHz and low voltage of <1 V operation

Li et al., Cell Reports Physical Science 3, 100711
January 19, 2022
https://doi.org/10.1016/j.xcrp.2021.100711

Cell Reports
Physical Science

CellPress
OPEN ACCESS

Article

A filterless organic photodetector electrically switchable between visible and infrared detection

Ning Li,[1] Naresh Eedugurala,[2] Jason D. Azoulay,[2] and Tse Nga Ng[1,3,*]

SUMMARY

Wavelength tunable detectors are essential for capturing spectral information within diverse applications such as those related to object recognition and identification. Here, we present a generalizable design for a compact dual-band photodetector based on the integration of two back-to-back organic photodiodes that respond to visible (400–700 nm) and infrared light (700–1,400 nm). The polarity under external bias provides the electronic switch between visible and infrared detection modes. Operating at a low voltage of <1 V, the organic photodetector exhibits a fast response with a −3-dB cutoff frequency of 18 kHz and specific detectivity of 7.8 × 10^9 Jones. The device provides contactless measurements of high temperatures that originated from blackbody radiation and spectroscopic dual-band imaging for object identification.

INTRODUCTION

Photodetectors with tunable spectral selectivity[1–4] are in high demand on account of the growing demands for capturing spectral information that improves object recognition and identification in many applications such as environmental surveillance, industrial inspection, autonomous navigation, and many others. External optical components such as filter wheels or diffraction gratings have been incorporated with photodetectors to discern signals in different spectral bands, but the external components render the detection system bulky and limit spectral scanning speed.

Recent developments have aimed to integrate spectral differentiation capabilities into the detector structure itself. Emerging designs, largely based on solution-processable semiconductors,[5–12] have demonstrated wavelength-selective photodetection. For example, the optical absorption characteristics were tuned in the photosensitive layer through charge collection narrowing[13,14] and the use of optical cavities,[15–17] which made it possible to achieve ultra-narrow band photodetection without external filters. Another approach changed the absorbing materials[4,18] within the detector to respond specifically to selected wavelengths. However, using these approaches results in detectors whose spectral sensitivity is fixed upon fabrication.

To realize filterless devices that are spectrally tunable following fabrication, researchers have explored electronic control mechanisms that toggle between photoactive layers, giving rise to dual-band detectors.[1–3,19,20] These devices are electrically switchable and respond to different spectral regions, offering the capability for color selection within the visible spectrum (i.e., to distinguish between blue and green light)[3] or switching between the visible and near-infrared (NIR) regions.[2] The dual-band structures are comprised of two photoactive layers with different

[1]Department of Electrical and Computer Engineering, University of California, San Diego, 9500 Gilman Drive, La Jolla, CA 92093-0407, USA

[2]Center for Optoelectronic Materials and Devices, School of Polymer Science and Engineering, The University of Southern Mississippi, 118 College Drive #5050, Hattiesburg, MS 39406, USA

[3]Lead contact

*Correspondence: tnn046@ucsd.edu

https://doi.org/10.1016/j.xcrp.2021.100711

spectral sensitivity arranged in a two-terminal stack, a simple structure that is advantageous for maximizing fill factor on readout integrated circuits. In prior work, the switching mechanisms have relied on rectification barriers that are specific to the chosen material sets.[1–3,19,20] However, we note that there is a generalizable concept underlying many of the rectification mechanisms, and it would be revealing to conceptualize a class of dual-band detectors by using the equivalent-circuit model of back-to-back diodes. This configuration of back-to-back diodes has been commonly used to address individual sensing elements within matrix arrays[21,22] and upconversion imagers.[23–26] Here, we clarify the operation of this device configuration in the context of spectrally tunable photodetectors to show how the electrical bias dictates which diode in the stack would generate a photoresponse under different operation conditions.

To apply the configuration of back-to-back diodes for dual-band detection, we use organic semiconductors[27–31] to demonstrate a detector that is switchable between the visible and the NIR to shortwave infrared (SWIR) regions. We examine the device operation as a function of external bias to characterize the detector performance in response to visible and infrared (IR) radiation. The voltage bias control allows rapid switching between visible and IR detection modes, enabling dual-band detection for spectroscopic sensing. For example, we demonstrate rapid differentiation between radiation sources such as the identification of an emerging fire threat or monitoring blackbody temperatures in industrial processes. The overall goal of this manuscript is to understand the device physics of the back-to-back diode model and reveal design rules for the detection of two arbitrary optical bands by choosing the appropriate stack of photoactive diodes.

RESULTS AND DISCUSSION

Device structure

The structure and materials of the dual-band detector are illustrated in Figures 1A and 1B, respectively. Poly(3-hexylthiophene-2,5-diyl) (P3HT) is the donor semiconducting polymer that is sensitive to visible light,[28] and poly(4-(5-(4-(3,5-bis(dodecyloxy)benzylidene)-4*H*-cyclopenta[2,1-*b*:3,4-*b'*]dithiophen-2-yl)thiophen-2-yl)-6,7-dioctyl-9-(thiophen-2-yl)-[1,2,5]thiadiazolo[3,4-*g*]quinoxaline)) (CDT-TQ) is the narrow bandgap donor that responds to SWIR light.[24,32,33] The small molecule [6,6]-phenyl-C71-butyric acid methyl ester ($PC_{71}BM$) acts as the acceptor in the bulk heterojunction (BHJ) layer. Energy level diagrams of the detector materials are included in Figure S1. The absorption spectra for the two BHJ films are shown in Figure 1C, with P3HT:$PC_{71}BM$ covering the visible region (wavelengths of 400—700 nm) and CDT-TQ:$PC_{71}BM$ spanning the NIR to SWIR from 700 to 1,400 nm.

The BHJ films were stacked in a back-to-back diode configuration as depicted in Figure 1D. The aluminum electrode was grounded, and either a positive or negative voltage was applied to the indium tin oxide (ITO) electrode. The polarity of the applied voltage placed one diode under reverse bias, whereas the other was under forward bias. The diode under reverse bias served as the active photodetector,[34,35] in which photogenerated charges could be collected, resulting in photocurrent generation. In the diode under forward bias, most of the photogenerated charges recombined (Figure 1E) and did not contribute to the photocurrent; the forward-biased diode was mainly a low resistance path for charge transport.

Characteristics of band switchable detector

The spectral responsivity of the detector under different applied voltages ($V_{applied}$) is shown in Figure 2A. Upon applying a positive voltage, we found that the detector

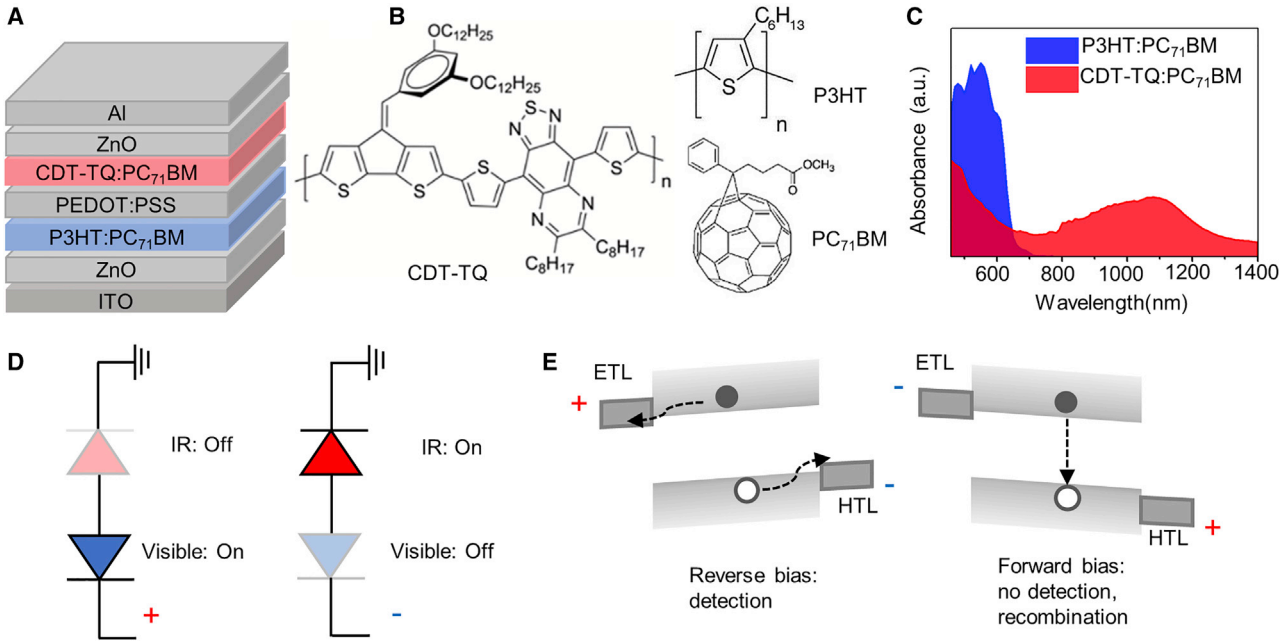

Figure 1. Device configurations

(A) A schematic of the dual-band photodetector.

(B) Molecular structures of semiconductors in the photodetector.

(C) Absorption spectra of bulk heterojunction layers.

(D) Switching between visible and IR detection according to bias polarities.

(E) Illustrations of charge generation and recombination in a photodiode under reverse and forward bias, respectively.

responsivity increased for wavelengths less than 650 nm in the visible. Conversely, application of a negative voltage led to higher responsivity in the NIR-SWIR from 700 nm to 1,400 nm. Thus, the detector was switchable in its response to either visible or IR light by controlling the bias polarity. The peak responsivity is 0.2 A/W in the visible band and 0.1 A/W in the IR band, which are similar to the values measured for individual photodiodes (Figure S2). These results indicate that the additional fabrication steps used to stack the diodes do not negatively affect device performance and that a small external bias (<1 V) was sufficient to extract photogenerated charges in the dual-band detector.

Figure 2B shows the current-voltage (IV) characteristics of the band-selective detector measured under light-emitting diodes (LEDs) for the two representative wavelengths of 600 nm (visible) and 1,050 nm (IR). For positive voltages, the P3HT:$PC_{71}BM$ layer was in reverse bias and active for visible wavelength detection consistent with the high photocurrent under 600 nm irradiation (blue data, Figure 1C). With the detector set to operate in visible detection mode, the photoresponse under 1,050 nm illumination was negligible. Alternatively, when the CDT-TQ:$PC_{71}BM$ layer was operated in reverse bias under negative voltages, the detector operated in IR detection mode and generated a photocurrent under 1,050 nm light (red data, Figure 1C), with a negligible response to 600 nm illumination.

The IV characteristics displayed different open-circuit voltages (V_{oc}) in the two operation modes, which were −0.4 V for the visible and 0.1 for the IR. These V_{oc} values matched those of individual diodes made with the corresponding BHJs by using similar light power (Figure S2). As is evident from the V_{oc} comparison, a built-in potential was retained in the integrated back-to-back diodes. Thus, the dual-band

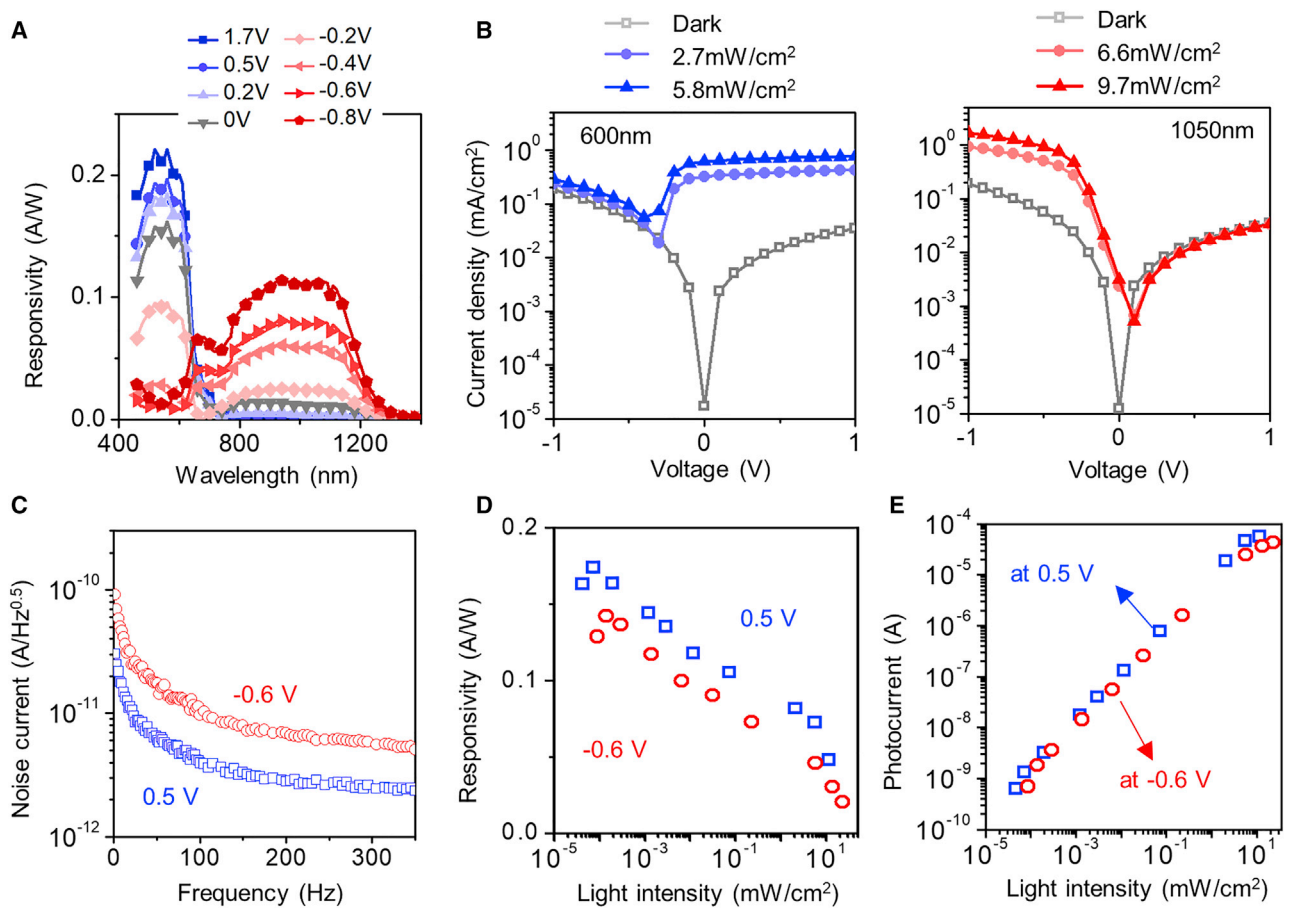

Figure 2. Device characteristics as a function of the applied voltage

(A) Responsivity versus wavelength of the dual-band detector under various applied voltages.

(B) Current-voltage characteristics of the detector under visible (600 nm) and IR (1050 nm) irradiation.

(C) Noise current spectra of the detector biased to operate in the visible detection mode ($V_{applied}$ = 0.5 V) and IR detection mode ($V_{applied}$ = −0.6 V).

(D and E) Responsivity (D) and photocurrent (E) versus incident light power. The light sources used in (D) and (E) were LEDs with peak emissions of 600 nm (blue squares) and 1,050 nm (red circles).

detector produced a photocurrent even at $V_{applied}$ = 0 V due to the non-zero built-in potential as shown in Figures 2A and 2B. The response at $V_{applied}$ = 0 V showed a lower responsivity than operation under an applied bias. Due to the net difference in V_{oc}, the detector with no external bias was more selective toward visible light than IR light. This feature, if desired, would enable single polarity switching (from zero to negative voltages, as opposed to bipolar switching from positive to negative voltages) that could be advantageous for low-power applications.[20]

The apparent difference in V_{oc} direction under visible and IR light (Figure 2B) is associated with the back-to-back configuration and charge generation process. Charge photogeneration occurs in different BHJs under visible and IR light, and charges are then driven by the built-in potential to be collected by respective electrodes. As shown in Figure 1D, the V_{oc} measured for the band-switchable detector under visible and IR light would be in the opposite direction, due to the back-to-back structure.

The bandgaps of the BHJ blends were dominating factors that defined the dark current in the dual-band photodetector. Generally, a wider bandgap is more effective at

resisting charge injection under reverse bias. Thus, the dark current was lower in visible detection mode because of the larger bandgap in the visible wavelength BHJ than that in the IR material combination. Likewise, the noise currents measured[36–38] by a spectral analyzer are shown in Figure 2C and exhibit lower noise levels when the detector is operating in visible detection mode, when compared to those in IR detection mode. To determine the specific detectivity (D^*) in each spectral band, we used the equation[36] $D^* = R\sqrt{A}/S_n$, where R is the responsivity, A is the active area, and S_n is the noise spectral density sampled at the same frequency as R. Based on data taken at 314 Hz in Figures 2A and 2C, the peak D^* was calculated to be 7.8×10^9 Jones in visible mode set with $V_{applied} = 0.5$ V and 1.2×10^9 Jones in the IR mode with $V_{applied} = -0.6$ V (the full spectral D^* is shown in Figure S3). The specific detectivity of the detector was slightly better in the visible than in the IR but was still the same order of magnitude so as to enable similarly effective detection in either operational mode.

It should be noted that the shot noise calculated from the dark current is 6.6×10^{-13} $A/\sqrt{Hz}$ at 0.5 V and 1.5×10^{-12} $A/\sqrt{Hz}$ at −0.6 V by using the assumption of $\sqrt{2qI_{dark}}$, where q is the elementary charge and I_{dark} is the dark current. The calculated shot noise is several times lower than the measured total noise contributions (2.5×10^{-12} $A/\sqrt{Hz}$ at 0.5 V and 5.5×10^{-12} $A/\sqrt{Hz}$ at −0.6 V, at 314 Hz). These results indicate that the total noise includes other noises such as thermal noise and 1/f noise. Simple estimation of total noise from shot noise would underestimate the noise level and thus overestimate the detectivity.

The detectivity is a key parameter for photodetectors, making it fair to compare different photosensing systems with various geometries. To improve the detectivity, it is promising to introduce photomultiplication,[39–41] where the responsivity can be substantially enhanced. Meanwhile, noise control is also critical because the noise level decides the minimum detectable light intensity. Strategies including interface control and active layer engineering have been developed.[6]

The photoresponse as a function of incident light power was also measured to examine the linearity and detection limits of the detector in the two spectral bands. The detector showed decreasing responsivity with increasing light power in Figure 2D, which is indicative of charge traps that increased the probability of recombination and reduced the photocurrent at high incident power. This characteristic stands in contrast to a trap-free device for which the responsivity would be independent of light power.

The responsivity of the diode based on CDT-TQ:$PC_{71}BM$ BHJ showed a dependence on the incident light intensity,[24] which indicates the existence of trap states in this IR diode. However, the responsivity for the P3HT:$PC_{71}BM$ diode showed less dependence on the incident light intensity (Figure S4). Thus, the intensity dependence of responsivity measured for the band-switchable detector is ascribed to traps in the IR diode.

Nonetheless, the detector was sensitive to a wide range of light power varying over six orders of magnitude. The lowest detectable power was 7.4×10^{-5} mW/cm^2 for the visible band and 1.4×10^{-4} mW/cm^2 for the IR band. The dynamic range (DR) is defined as $DR = 10\log(P_{max}/P_{min})$, where the P_{max} and P_{min} represent the maximum and minimum incident power levels between which the photodetector response was linear. Based on Figure 2E, the DR in the visible and IR detection modes are estimated to be 49 dB and 46 dB, respectively.

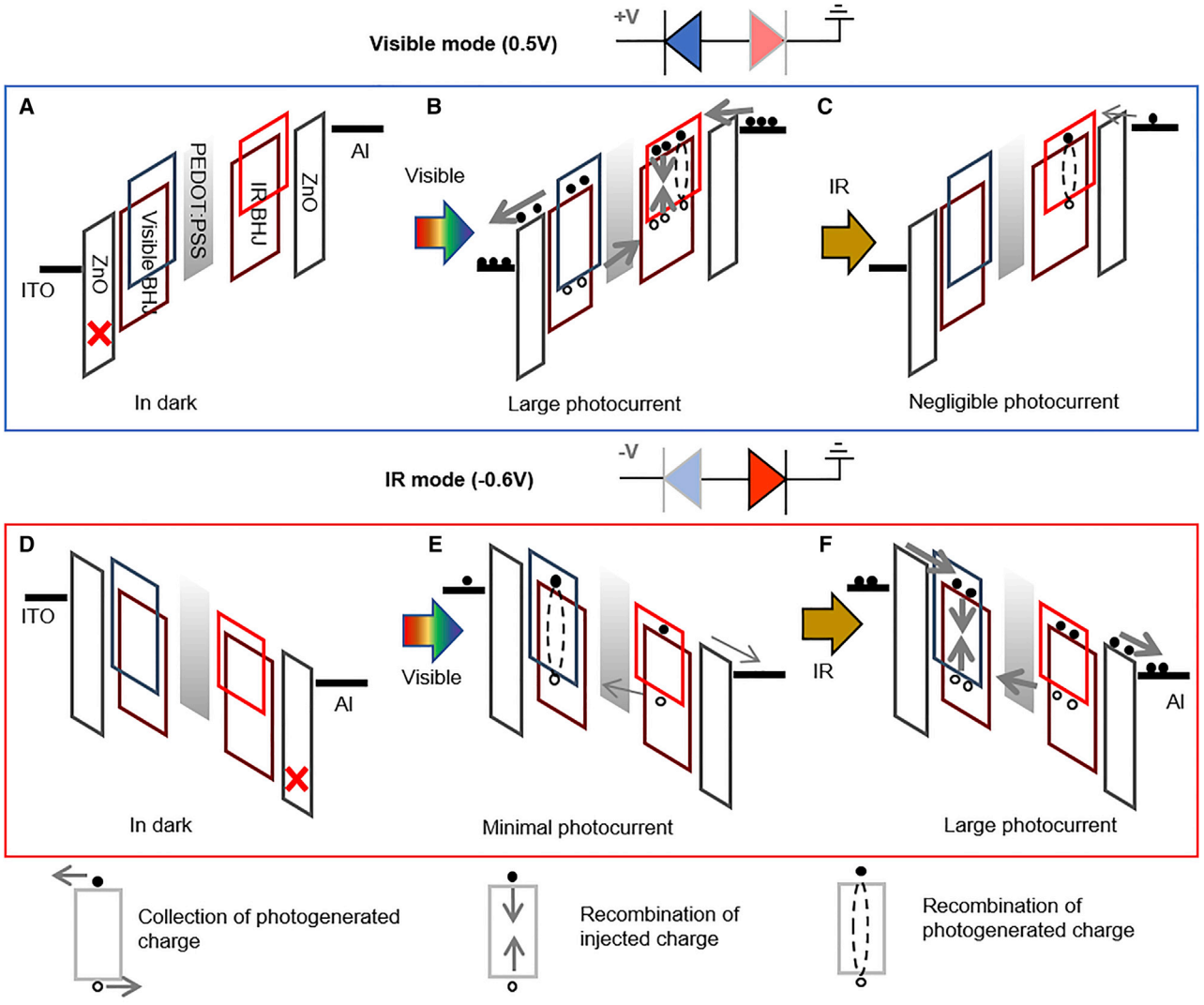

Figure 3. The working mechanisms of the photodetector

Under positive (A–C) and negative bias (D–F). The diagrams correspond to conditions of being in the dark (A and D), under visible light (B and E), and under IR light (C and F).

Mechanism of band-switchable detection

Figure 3 illustrates the working principles that enable spectrally tunable detection and compares carrier dynamics in response to the bias polarity and incident spectral bands. In the dark, the current flow was low due to a high barrier blocking hole injection in the reverse-biased diode (Figures 3A and 3D). While under illumination, the dual-band detector responded to visible and IR wavelengths differently. In particular, the successful collection of photogenerated charges required the applied voltage to assist current flow across the two diode layers. For example, when the applied bias was positive, photogenerated charges in the two BHJs traversed different pathways. Under visible light, photogenerated electrons from the P3HT:$PC_{71}BM$ BHJ were collected through the n-type ZnO interlayer, whereas holes were transported through the p-type PEDOT:PSS interlayer, which then recombined with injected electrons from the Al electrode to complete the current flow. There was a recombination of photogenerated electron-hole pairs in the IR diode under

forward bias, but overall, the photocurrent was large as depicted in Figure 3B. In contrast, under IR light, there was a negligible photocurrent with the detector set in visible detection mode. The absorption of IR light occurred in the IR BHJ layer, but the forward bias resulted in recombination of the photogenerated electron-hole pairs, which precluded their collection as depicted in Figure 3C. As such, the detector was sensitive only to visible light when set in visible detection mode.

By changing to a negative applied voltage, the detection band was switched from the visible to the IR band. In IR detection mode, the IR diode was reverse-biased, whereas the visible diode was forward- biased. Under visible light, there were photogenerated charges in both BHJ layers; but in the visible BHJ layer, the external field aided recombination over charge extraction as shown in Figure 3E. Moreover, the detector was designed to absorb most of the visible light in the P3HT:$PC_{71}BM$ layer so that less than 30% of the visible light was transmitted to the IR layer (Figure S5). Because visible photons were mostly blocked from reaching the IR layer, only a small population of charge was generated, consistent with the low responsivity to visible light when the detector was operating in IR detection mode (Figure 2A). Characterization of the detector by electrochemical impedance spectroscopy[42] (Figure S6) corroborated that there was only a small change in charge density under visible light. Meanwhile, under IR light, the detector generated and extracted charges efficiently, as shown in Figure 3F. Due to their longer wavelengths, IR photons were able to penetrate through the visible BHJ, which showed IR transmission of up to 90% (Figure S5). The photogenerated charges were then transported through the forward-biased visible diode, producing a large photocurrent. These properties facilitate the operation of the dual-band detector, which is effective at selective charge collection for the chosen spectral band.

It is worth noting that the dual-band photodetector incorporated both electronic and optical effects. The thickness of BHJ layers, particularly for the layer that first encounters incident light, affects the transmission of light to the subsequent layer. We have examined this optical filtering effect by increasing the thickness of the visible BHJ layer. As the P3HT:$PC_{71}BM$ film thickness is increased from 140 nm to 210 nm, the photocurrent decreased as a result of diminished charge collection through the thicker diode (Figure S7). We believe that the diminished charge collection was due to bulk recombination within the device because charges moved a longer distance before being collected by the electrodes, during which the recombination rate increased in our structure. In our process, the reduction in photoresponse in the thicker P3HT:$PC_{71}BM$ BHJ device outweighed the benefit from increased visible light absorption or filtering, and we did not adjust the thickness further. However, we note that future optimization can be done, through improved processing and optical simulations to design layer thicknesses.[43]

Moreover, the BHJ materials can be substituted to adjust the absorption range. For example, we demonstrated the use of another BHJ combination in Figure S8 to change the spectral window and focus on the NIR instead of the SWIR spectral region. These results indicated that the combination of two BHJs in a back-to-back configuration is viable in achieving band-tunable photodetection. Regarding design considerations affecting electrical properties, the built-in potential of the diodes and the interfacial charge transport layers are parameters that control the magnitude of external bias needed to switch between the two detection bands. Regarding optical designs, the BHJ sensitive to short wavelengths should be placed in front of the BHJ that is sensitive to long wavelengths, such that the long-wavelength photons can pass through the front BHJ and be detected by the rear BHJ. The thickness for the front BHJ film requires a balance between optical absorption and electrical

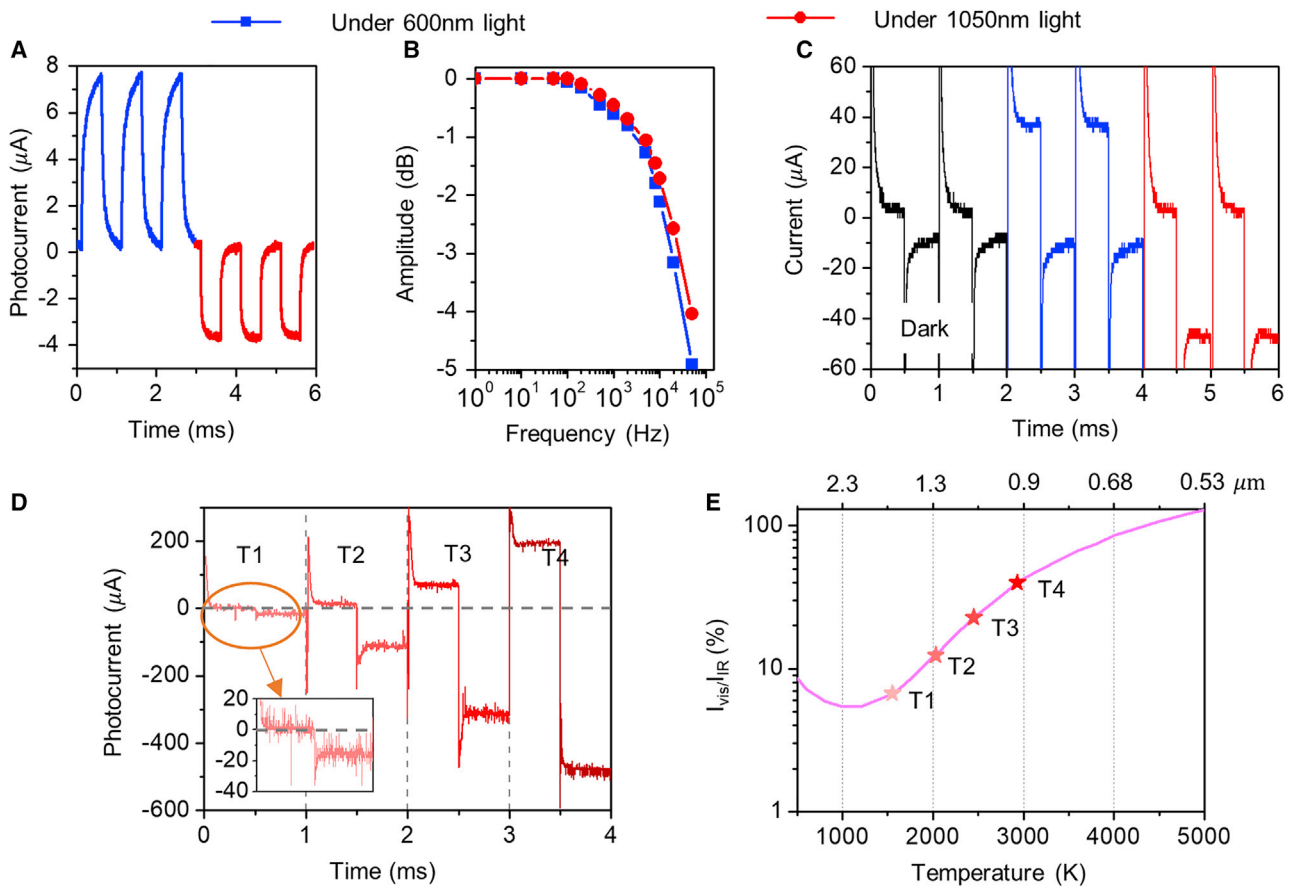

Figure 4. Rapid device response

(A) The transient response of the detector biased at 0.5 V for visible light detection during 0–3 ms and at −0.6 V for IR detection during 3–6 ms. The incident light was modulated at 1 kHz.

(B) Signal amplitude versus the modulation frequency of incident light.

(C) Electrical modulation of the detector biased at either 0.5 V or −0.6 V, each for a 0.5-ms period. The colors indicated measurements in the dark (black), or under constant irradiation of visible 600 nm or IR 1,050 nm light from LEDs.

(D) Detector current recorded under a tungsten lamp operating at four different temperatures. Same as in (C), the detector is alternatively switched between visible and IR detection modes every 0.5 ms.

(E) Ratio of current measured under 0.5 V (visible detection mode) to current under −0.6 V (IR detection mode). The star symbols are data from (D), and the line represents the calculated ratio based on Equation 1. The top axis shows the wavelengths of peak emission corresponding to blackbodies at different temperatures.

transport. The front BHJ film should be thick enough to absorb most of the incoming short-wavelength photons to avoid the response in the rear BHJ. Yet, charge transport and collection would be reduced once the front BHJ becomes too thick. Incorporating a resonance cavity or optical spacers can be future options for manipulating optical interferences through which the film absorption can be enhanced while the thickness of the active layer remains the same.

Rapid spectroscopic photodetection and imaging

By simply changing the applied voltage of the detector, the electronic control allowed rapid switching between detection bands and facilitated a large sampling bandwidth. The transient photoresponse in Figure 4A shows that the signal rise time was 270 μs in visible detection mode and 167 μs in IR mode. The difference in response speeds originated from a smaller shunt resistance in the IR BHJ than that in the visible BHJ under reverse bias (Figure S6). The −3-dB cutoff frequencies

of the detector were measured in Figure 4B to be 18 kHz and 25 kHz for visible and IR detection modes, respectively. Figures 4A and 4B show modulation of the incident light, whereas Figures 4C and 4D show measurements in which the applied voltage was modulated while the incident light was constant. The applied voltage was either 0.5 V or −0.6 V, switched every 0.5 ms to set the detector in visible or IR detection mode, respectively. The dark current (black line) was higher in IR mode than that in visible detection mode, in accordance with the IV characteristics in Figures 2B and 2C. The positive increase in current (blue line) was a response to incident visible light, and the increase in the negative direction (red line) was due to IR irradiation. There was overshot current whenever the voltage was switched due to parasitic capacitance during charging/discharge of the multilayer structure. (Figures 4C and 4D were switched at 1 kHz, but for Figure 4A, the voltage was not switched at high speed and only the light source was modulated. With no switching of bias, Figure 4A did not show parasitic capacitance spikes.) The current quickly settled to the baseline by 70 μs in Figure 4C. Thus, the switch between detection modes was achievable at high speed in the tens of kHz.

Figure 4D shows the photocurrent measured for visible and IR detection modes under a tungsten lamp emitting as a blackbody radiator at different temperatures, as the lamp current was adjusted. The ratio of current between the two detection modes shifted depending on the temperature of the tungsten lamp. By providing the current ratio (I_{vis}/I_{IR}), the dual-band detector enabled the non-contact measurement of the temperature of a blackbody radiator, which is particularly useful for high-temperature ranges in industrial processes such as remote monitoring of furnaces to ensure environmental safety. The distribution of visible photons and IR photons emitted from a blackbody is different when its temperature varies, as described by Planck's laws (Figure S9).[44] The photocurrent of the detector is proportional to the integrand of responsivity and spectral radiance over the spectrum of the detection band. A comparison of the photocurrent under visible versus IR detection modes provides clues to characteristics of the light source and allows inference of the temperature according to the ratio of spectral radiance, $L(\lambda,T)$:

$$\frac{I_{vis}}{I_{IR}} = \int R_{vis}(\lambda)\cdot L(\lambda,T)d\lambda \Big/ \int R_{IR}(\lambda)\cdot L(\lambda,T)d\lambda$$

$$\text{with } L(\lambda,\ T) = \frac{2hc^2}{\lambda^5}\left[\exp\left(\frac{hc}{\lambda kT}\right) - 1\right]^{-1} \qquad \text{(Equation 1)}$$

where $R_{vis}(\lambda)$ and $R_{IR}(\lambda)$ are the responsivities in the visible and IR detection mode of the detector, λ is the wavelength, T is the temperature, h is the Planck's constant, c is the velocity of light, and k is the Boltzmann constant. We calculated the ratio using a range that covers the 400 nm to 1,400 nm detection window of the detector. The projected I_{vis}/I_{IR} ratio as a function of blackbody temperature is presented in Figure 4E (red line). In this estimation, I_{vis}/I_{IR} increases with temperature in a high-temperature region, e.g., 1,200 K—5,000 K. In this work, the use of this ratio is not applicable for estimating temperatures of <1,200 K, as the emission peak is shifted to mid-IR wavelengths beyond the SWIR band limit of the detector here. The four values of I_{vis}/I_{IR} in Figure 4D were extracted and plotted over the calculated I_{vis}/I_{IR} line in Figure 4E. The blackbody temperature corresponding to the four irradiation conditions were thus estimated to be T1 = 1,600 K, T2 = 2,100 K, T3 = 2,500 K, and T4 = 3,000 K. As an independent verification, the temperature values were checked using the emission spectra of the tungsten lamp operated at corresponding current settings in Figure S10. The temperature values are in good agreement with those extracted in Figure 4E.

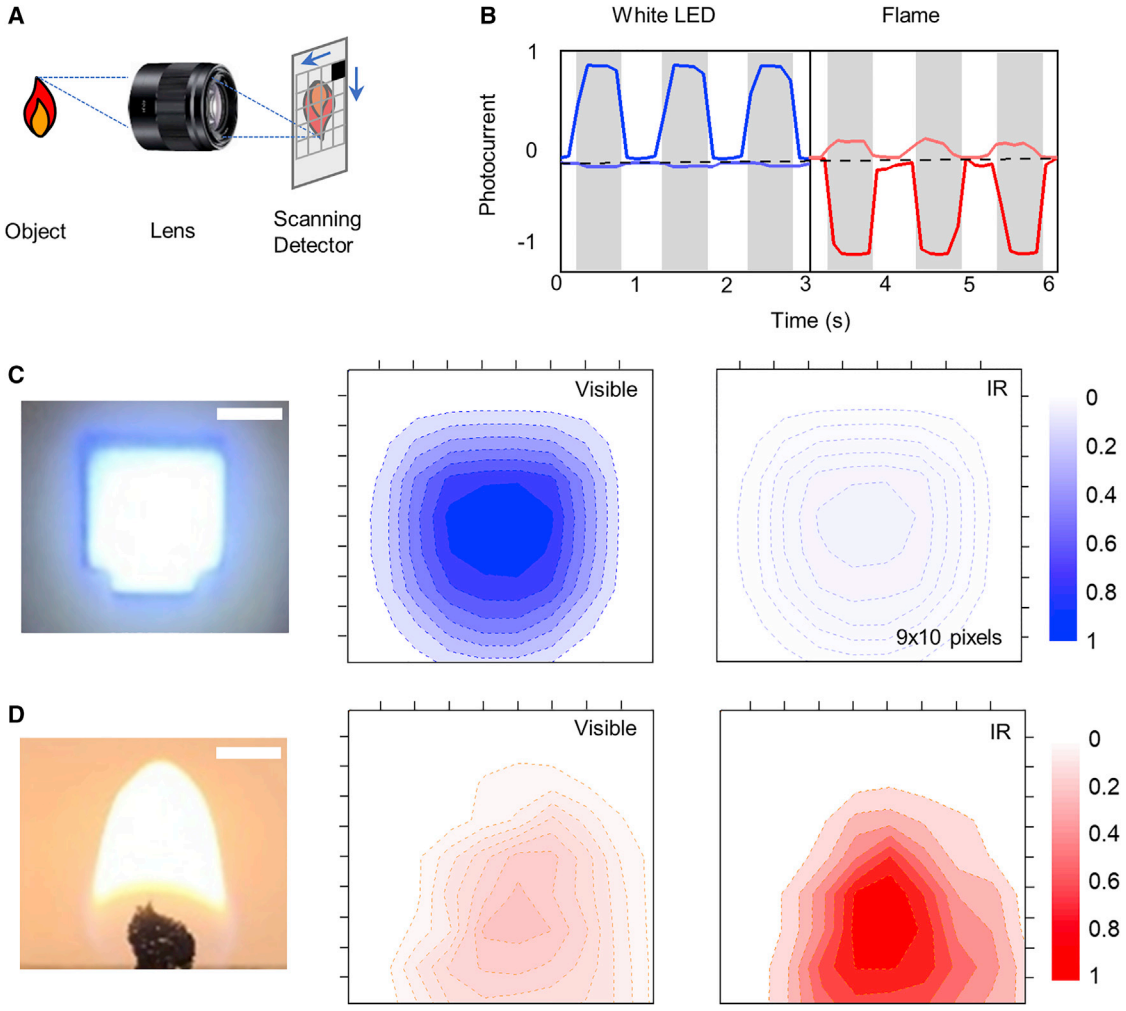

Figure 5. Demonstration of spectroscopic imaging

(A) The imaging setup included a fixed optical lens and a moving stage to scan the detector (denoted by the black square) at the focal plane of the lens. The optical lens has a magnification of 1.5×.

(B) Normalized photocurrent of the detector under the irradiation of a white LED or a candle flame. The detector was fixed at either 0.5 V (left) or −0.6 V (right), whereas the LED or the candle-light beam was modulated through an optical chopper at 1 Hz, for which gray regions were under the light. The positive current represents visible response, whereas the negative current represents IR response.

(C) Photograph of a white LED and the corresponding spatial maps of normalized visible and IR signals.

(D) Photograph of a candle flame and the corresponding spatial maps of normalized visible and IR signals. The scale bars in the photographs represent 0.5 cm.

In another demonstration, the dual-band detector was used to quickly scan over an area and distinguish the difference in emission spectra between light sources. This imaging capability could be applied to environmental monitoring such as identifying the location of an emerging fire threat. The setup for imaging is schematically depicted in Figure 5A, in which the detector was placed on a programmable stage on the focal plane of a fixed lens. In our setup, the detector (3×3 mm^2) was moved to record over a matrix of 9×10 locations that covered the 3×3 cm^2 area so as to reproduce images of the scanned area and separate signal contributions from both visible and IR light. Two light sources were used as the object for the spectroscopic imaging experiments, namely, one a white LED and the other a candle flame. Figure 5B presents the normalized photocurrent of the detector illuminated by the white LED or candle flame, with the light path modulated by an optical chopper at

1 Hz. The current measurement showed a photoresponse predominantly in the visible mode for the LED. The magnitude of this signal was 19-fold higher in the visible than that in the IR, as determined from the normalized current (i.e., the current was normalized by the highest photocurrent, measured to be 7.7 μA). For the candle flame, the photoresponse was predominantly in the IR for the candle flame (current normalized by dividing by 470 nA).

The spatial maps of the photocurrent are shown in Figure 5C for the LED and Figure 5D for the candle flame by using the same normalization factors as in Figure 5B. For the images, the applied voltage was set to the desired detection mode (either 0.5 V or −0.6V) throughout the imaging scan. The image contrast demonstrated that the emission spectra from the white LED lighting system is different than that from a fire. When compared to traditional fire alarms based on an ionizing smoke sensor, the demonstrations here provided complementary information about a fire size and radiation temperature through an analysis of the light spectra within the scanned area. Besides monitoring incident light power, the dual-band detector offered additional spectroscopic characterization that extends beyond the capability of conventional filterless photosensors. In addition, the back-to-back diode configuration is compatible with direct integration on pixelated matrix backplanes, offering opportunities to pair visible-blind IR detection with red, green, or blue detection bands and extend this architecture to multispectral imaging in the future.

In this work, we presented design guidelines and device physics of an organic dual-band photodetector that is switchable between visible and IR light measurements at tens of kHz. The rapid response was enabled by simple voltage control on the back-to-back diodes, a generalizable configuration that can easily be adopted for different materials combinations to achieve target spectral sensitivity for each band. The switch between spectral bands was completed at low voltage (<1 V) with a specific detectivity up to 7.8×10^9 Jones. The compact photodetector provided spectroscopic information for the inference of blackbody temperature and object identification. The generality of this dual-band design is applicable to the vast array of solution-processed organic semiconductors and extendable to colloidal quantum dots or solution-processed perovskites. This information will facilitate easy tuning of the detector spectral band over a broad range from visible to IR wavelengths for multispectral imaging applications.

EXPERIMENTAL PROCEDURES

Resource availability

Lead contact

Further information and requests for resources should be directed to and will be fulfilled by the lead contact, Tse Nga Ng (tnn046@ucsd.edu).

Materials availability

This study did not generate new unique reagents.

Data and code availability

All the data supporting the findings of this study are presented in the paper and the supplemental information. Other data are available from the lead contact upon reasonable request. This study did not generate any code.

Materials used in this research

The donor polymer P3HT and acceptors $PC_{71}BM$ and ITIC-M were purchased from Ossila, and CDT-TQ was synthesized as reported in reference.[22] PEDOT:PSS was

purchased from Heraeus (CLEVIOS P VP AI 4083). The ZnO layer was prepared according to the method described by Womelsforf.[45] The surfactant was ordered from Chemours (Capstone FS-31). All materials were used as received without any further treatment.

Device fabrication

Pre-patterned ITO substrates were cleaned ultrasonically in detergent, deionized water, acetone, and isopropanol sequentially for 10 min each. The substrates were then dried in the oven. The ZnO nanoparticle solution was spin-coated in a glovebox to form a thin electron transport interlayer. After the substrates were dry, a mixed P3HT:$PC_{71}BM$ solution (weight ratio of 1:1) at a concentration of 20 mg/mL was spin-coated onto the ZnO layer. The thickness of the P3HT:$PC_{71}BM$ layer was 140 nm. The P3HT:$PC_{71}BM$ layer was annealed at a temperature of 120°C for 10 min. The surfactant was blended with the PEDOT:PSS at a volume ratio of 1:150 to reduce the surface energy of the P3HT:$PC_{71}BM$ layer. Then, a 55-nm-thick PEDOT:PSS layer was spin-coated onto the P3HT:$PC_{71}BM$ BHJ outside of the glovebox. The PEDOT:PSS layer was then annealed at 120°C for another 10 min. The top BHJ layer was deposited by spin-coating a CDT-TQ:$PC_{71}BM$ (weight ratio of 1:2) solution with a concentration of 24 mg/mL in the glovebox to give a thickness of 160 nm. Next, a thin ZnO layer was prepared by spin coating on top of the device stack. Finally, a 100 nm Al electrode was thermally evaporated in a vacuum through shadow masks defining an active area of 0.1 cm^2. For a comparison between the dual-band and single-band detectors, the structures for individual photodiodes were ITO/ZnO/P3HT:$PC_{71}BM$/PEDOT:PSS/Ag for the visible band and ITO/PEDOT:PSS/CDT-TQ:$PC_{71}BM$/ZnO/Al for the SWIR band. The devices were encapsulated with glass slides before characterization.

Spectral response measurements

The spectral photoresponse was measured under monochromatic light (modulated at 314 Hz with an optical chopper) from a tungsten lamp combined with a monochromator (Spectral Products). The photocurrent was amplified by a low-noise current amplifier (Stanford Research Systems, SR 570) and then recorded by a lock-in (Stanford Research Systems, SR 530) amplifier. The bias on the device was provided by the low-noise current amplifier.

Current-voltage measurements

The current-voltage characteristics were recorded using an electrometer (Keithley 2400) controlled by a LABVIEW program. The visible (600 nm) and IR light (1050 nm) were provided by two LEDs from Thorlabs. The noise current of the detector operated in different modes was amplified by the low-noise current amplifier and then recorded by a spectrum analyzer (HP 89410A). The spectrum analyzer recorded the noise voltage, and the noise current of the device was calculated by converting voltage to current based on the sensitivity of the current amplifier. The impedance and capacitance data as a function of frequency was characterized using a potentiostat (BioLogic SP-200). The responsivity (in units of ampere/watt) is calculated by $R = I_{ph}/P_{in}$, where I_{ph} is the photocurrent and P_{in} is the incident light power.

In the transient response measurements, the detector was biased at either 0.5 V or −0.6 V, whereas the light signal was from two LEDs driven by a function generator (RIGOL, DG2041A), modulated at 1 kHz. The transient current generated in the detector was collected and amplified by the preamplifier and then displayed on an oscilloscope (RIGOL, DS1102E).

Spectroscopic imaging demonstrations

In spectroscopic measurements, the band-switchable detector was driven by a function generator applying voltage bias alternatively, at 0.5 V and −0.6 V. The tungsten lamp was operated at different temperatures by controlling the drive current.

In the imaging demonstration, the photodetector was mounted to a 2-dimensional (2D) optical stage that moves freely in a 2D plane. The light signal from either the white LED (0.5 mW/cm^2) or the candle flame (0.05 mW/cm^2) was focused by an optical lens to form an image on the 2D plane. The detector with an area of 3 × 3 mm^2 operated either in visible mode (0.5V) or IR mode (−0.6V) to scan an area of 3 × 3 cm^2 and record the light signal at different positions. The photocurrent is a function of operation mode and position in the 2D plane.

SUPPLEMENTAL INFORMATION

Supplemental information can be found online at https://doi.org/10.1016/j.xcrp.2021.100711.

ACKNOWLEDGMENTS

The authors N.L. and T.N.N. acknowledge support from Samsung Advanced Institute of Technology. N.E. and J.D.A. acknowledge support from the National Science Foundation (OIA-1757220).

AUTHOR CONTRIBUTIONS

N.L. and T.N.N. conceived the idea, designed the experiments, and analyzed the data. N.L. carried out the fabrication and measurement of the devices. N.E. synthesized the SWIR polymer under the supervision of J.D.A. All authors contributed to discussions and writing of the manuscript.

DECLARATION OF INTERESTS

The authors declare no competing financial interests.

Received: October 27, 2021
Revised: November 14, 2021
Accepted: December 8, 2021
Published: January 5, 2022

REFERENCES

1. Tang, X., Ackerman, M.M., Chen, M., and Guyot-Sionnest, P. (2019). Dual-band infrared imaging using stacked colloidal quantum dot photodiodes. Nat. Photonics *13*, 277–282.

2. Lan, Z., Lei, Y., Chan, W.K.E., Chen, S., Luo, D., and Zhu, F. (2020). Near-infrared and visible light dual-mode organic photodetectors. Sci. Adv. *6*, eaaw8065.

3. Lan, Z., and Zhu, F. (2021). Electrically Switchable Color-Selective Organic Photodetectors for Full-Color Imaging. ACS Nano *15*, 13674.

4. Strobel, N., Droseros, N., Köntges, W., Seiberlich, M., Pietsch, M., Schlisske, S., Lindheimer, F., Schröder, R.R., Lemmer, U., Pfannmöller, M., et al. (2020). Color-Selective Printed Organic Photodiodes for Filterless Multichannel Visible Light Communication. Adv. Mater. *32*, e1908258.

5. García De Arquer, F.P., Armin, A., Meredith, P., and Sargent, E.H. (2017). Solution-processed semiconductors for next-generation photodetectors. Nat. Rev. Mater. *2*, 16100.

6. Li, N., Mahalingavelar, P., Vella, J.H., Leem, D.S., Azoulay, J.D., and Ng, T.N. (2021). Solution-processable infrared photodetectors: Materials, device physics, and applications. Mater. Sci. Eng. Rep. *146*, 100643.

7. Wu, Z., Zhai, Y., Kim, H., Azoulay, J.D., and Ng, T.N. (2018). Emerging Design and Characterization Guidelines for Polymer-Based Infrared Photodetectors. Acc. Chem. Res. *51*, 3144–3153.

8. Baeg, K.J., Binda, M., Natali, D., Caironi, M., and Noh, Y.Y. (2013). Organic light detectors: photodiodes and phototransistors. Adv. Mater. *25*, 4267–4295.

9. Bonnassieux, Y., Brabec, C.J., Cao, Y., Carmichael, T.B., Chabinyc, M.L., Cheng, K., Cho, G., Chung, A., Cobb, C.L., Distler, A., et al. (2021). The 2021 Flexible and Printed Electronics Roadmap. Flex. Print. Electron. *6*, 023001.

10. Wang, W., Du, M., Zhang, M., Miao, J., Fang, Y., and Zhang, F. (2018). Organic Photodetectors with Gain and Broadband/Narrowband Response under Top/Bottom Illumination Conditions. Adv. Opt. Mater. *6*, 1800249.

11. Wang, K., Huang, L., Eedugurala, N., Zhang, S., Sabuj, M.A., Rai, N., Gu, X., Azoulay, J.D., and Ng, T.N. (2019). Wide Potential Window Supercapacitors Using Open-Shell Donor–Acceptor Conjugated Polymers with Stable N-Doped States. Adv. Energy Mater. *9*, 1902806.

12. Zhai, Y., Wang, Z., Kwon, K.S., Cai, S., Lipomi, D., and Ng, T.N. (2020). Printing Multi-Material

Organic Haptic Actuators. Adv. Mater. *33*, 2002541.

13. Armin, A., Jansen-van Vuuren, R.D., Kopidakis, N., Burn, P.L., and Meredith, P. (2015). Narrowband light detection via internal quantum efficiency manipulation of organic photodiodes. Nat. Commun. *6*, 6343.

14. Lin, Q., Lin, Q., Armin, A., Burn, P.L., and Meredith, P. (2015). Filterless narrowband visible photodetectors. Nat. Photonics *9*, 687.

15. Siegmund, B., Mischok, A., Benduhn, J., Zeika, O., Ullbrich, S., Nehm, F., Böhm, M., Spoltore, D., Fröb, H., Körner, C., et al. (2017). Organic narrowband near-infrared photodetectors based on intermolecular charge-transfer absorption. Nat. Commun. *8*, 15421.

16. Yazmaciyan, A., Meredith, P., and Armin, A. (2019). Cavity Enhanced Organic Photodiodes with Charge Collection Narrowing. Adv. Opt. Mater. *7*, 1801543.

17. Yang, J., Huang, J., Li, R., Li, H., Sun, B., Lin, Q., Wang, M., Ma, Z., Vandewal, K., and Tang, Z. (2021). Cavity-Enhanced Near-Infrared Organic Photodetectors Based on a Conjugated Polymer Containing [1,2,5]Selenadiazolo [3,4- c]Pyridine. Chem. Mater. *33*, 5147–5155.

18. Kim, J., Kwon, S.M., Kang, Y.K., Kim, Y.H., Lee, M.J., Han, K., Facchetti, A., Kim, M.G., and Park, S.K. (2019). A skin-like two-dimensionally pixelized full-color quantum dot photodetector. Sci. Adv. *5*, eaax8801.

19. Haddadi, A., Chevallier, R., Chen, G., Hoang, A.M., and Razeghi, M. (2015). Bias-selectable dual-band mid-/long-wavelength infrared photodetectors based on InAs/InAs1-xSbx type-II superlattices. Appl. Phys. Lett. *106*, 011104.

20. Li, L., Chen, H., Fang, Z., Meng, X., Zuo, C., Lv, M., Tian, Y., Fang, Y., Xiao, Z., Shan, C., et al. (2020). An Electrically Modulated Single-Color/ Dual-Color Imaging Photodetector. Adv. Mater. *32*, e1907257.

21. Ko, H.C., Stoykovich, M.P., Song, J., Malyarchuk, V., Choi, W.M., Yu, C.J., Geddes, J.B., 3rd, Xiao, J., Wang, S., Huang, Y., and Rogers, J.A. (2008). A hemispherical electronic eye camera based on compressible silicon optoelectronics. Nature *454*, 748–753.

22. Wu, Z., Zhai, Y., Yao, W., Eedugurala, N., Zhang, S., Huang, L., Gu, X., Azoulay, J.D., and Ng, T.N. (2018). The Role of Dielectric Screening in Organic Shortwave Infrared Photodiodes for Spectroscopic Image Sensing. Adv. Funct. Mater. *28*, 1805738.

23. Li, N., Lau, Y.S., Xiao, Z., Ding, L., and Zhu, F. (2018). NIR to Visible Light Upconversion Devices Comprising an NIR Charge Generation Layer and a Perovskite Emitter. Adv. Opt. Mater. *6*, 1801084.

24. Li, N., Eedugurala, N., Leem, D.S., Azoulay, J.D., and Ng, T.N. (2021). Organic Upconversion Imager with Dual Electronic and Optical Readouts for Shortwave Infrared Light Detection. Adv. Funct. Mater. *31*, 2100565.

25. Li, N., Lan, Z., Lau, Y.S., Xie, J., Zhao, D., and Zhu, F. (2020). SWIR Photodetection and Visualization Realized by Incorporating an Organic SWIR Sensitive Bulk Heterojunction. Adv. Sci. (Weinh.) *7*, 2000444.

26. Liu, S.W., Lee, C.C., Yuan, C.H., Su, W.C., Lin, S.Y., Chang, W.C., Huang, B.Y., Lin, C.F., Lee, Y.Z., Su, T.H., and Chen, K.T. (2015). Transparent organic upconversion devices for near-infrared sensing. Adv. Mater. *27*, 1217–1222.

27. Vella, J.H., Huang, L., Eedugurala, N., Mayer, K.S., Ng, T.N., and Azoulay, J.D. (2021). Broadband infrared photodetection using a narrow bandgap conjugated polymer. Sci. Adv. *7*, abg2418.

28. Fuentes-Hernandez, C., Chou, W.F., Khan, T.M., Diniz, L., Lukens, J., Larrain, F.A., Rodriguez-Toro, V.A., and Kippelen, B. (2020). Large-area low-noise flexible organic photodiodes for detecting faint visible light. Science *370*, 698–701.

29. Leem, D.S., Lee, K.H., Li, N., Park, B.W., Choi, T., Ro, T., Kwon, O.K., Kwon, Y.N., Ng, T.N., and Kim, S. (2020). Highly Responsive and Thermally Reliable Near-Infrared Organic Photodiodes Utilizing Naphthalocyanine Molecules Tuned with Axial Ligands. Adv. Opt. Mater. *9*, 2001682.

30. Gasparini, N., Gregori, A., Salvador, M., Biele, M., Wadsworth, A., Tedde, S., Baran, D., McCulloch, I., and Brabec, C.J. (2018). Visible and Near-Infrared Imaging with Nonfullerene-Based Photodetectors. Adv. Mater. Technol. *3*, 1800104.

31. Farahat, M.E., Laventure, A., Anderson, M.A., Mainville, M., Tintori, F., Leclerc, M., Ratcliff, E.L., and Welch, G.C. (2020). Slot-Die-Coated Ternary Organic Photovoltaics for Indoor Light Recycling. ACS Appl. Mater. Interfaces *12*, 43684–43693.

32. Li, N., Lim, J., Azoulay, J.D., and Ng, T.N. (2020). Tuning the charge blocking layer to enhance photomultiplication in organic shortwave infrared photodetectors. J. Mater. Chem. C Mater. Opt. Electron. Devices *8*, 15142–15149.

33. Wu, Z., Li, N., Eedugurala, N., Azoulay, J.D., Leem, D.-S., and Ng, T.N. (2020). Noise and detectivity limits in organic shortwave infrared photodiodes with low disorder. npj Flexible Electronics *4*, 6.

34. Li, N., Lau, Y.S., Miao, Y., and Zhu, F. (2018). Electroluminescence and photo-response of inorganic halide perovskite bi-functional diodes. Nanophotonics *7*, 1981–1988.

35. Bao, C., Xu, W., Yang, J., Bai, S., Teng, P., Yang, Y., Wang, J., Zhao, N., Zhang, W., Huang, W., and Gao, F. (2020). Bidirectional optical signal transmission between two identical devices using perovskite diodes. Nat. Electron. *3*, 156–164.

36. Fang, Y., Armin, A., Meredith, P., and Huang, J. (2019). Accurate characterization of next-generation thin-film photodetectors. Nat. Photonics *13*, 1–4.

37. Wu, Z., Yao, W., London, A.E., Azoulay, J.D., and Ng, T.N. (2018). Elucidating the Detectivity Limits in Shortwave Infrared Organic Photodiodes. Adv. Funct. Mater. *28*, 1800391.

38. Huang, J., Lee, J., Nakayama, H., Schrock, M., Cao, D.X., Cho, K., Bazan, G.C., and Nguyen, T.Q. (2021). Understanding and Countering Illumination-Sensitive Dark Current: Toward Organic Photodetectors with Reliable High Detectivity. ACS Nano *15*, 1753–1763.

39. Guo, F., Yang, B., Yuan, Y., Xiao, Z., Dong, Q., Bi, Y., and Huang, J. (2012). A nanocomposite ultraviolet photodetector based on interfacial trap-controlled charge injection. Nat. Nanotechnol. *7*, 798–802.

40. Li, L., Zhang, F., Wang, J., An, Q., Sun, Q., Wang, W., Zhang, J., and Teng, F. (2015). Achieving EQE of 16,700% in P3HT:PC71BM based photodetectors by trap-assisted photomultiplication. Sci. Rep. *5*, 9181.

41. Wu, Y.L., Fukuda, K., Yokota, T., and Someya, T. (2019). A Highly Responsive Organic Image Sensor Based on a Two-Terminal Organic Photodetector with Photomultiplication. Adv. Mater. *31*, e1903687.

42. Street, R.A., Yang, Y., Thompson, B.C., and McCulloch, I. (2016). Capacitance Spectroscopy of Light Induced Trap States in Organic Solar Cells. J. Phys. Chem. C *120*, 22169–22178.

43. Dang, M.T., Hirsch, L., and Wantz, G. (2011). P3HT:PCBM, best seller in polymer photovoltaic research. Adv. Mater. *23*, 3597–3602.

44. Rogalski, A. (2019). Infrared and Terahertz Detectors (CRC Press).

45. Womelsdorf, H.-J. (2000). US patent US6710091B1.